Chemical Science

ROYAL SOCIETY OF CHEMISTRY

EDGE ARTICLE

View Article Online
View Journal | View Issue

Cite this: *Chem. Sci.*, 2025, **16**, 2850

All publication charges for this article have been paid for by the Royal Society of Chemistry

Design of a new Ni@NCNT/graphene hybrid structured catalyst for high-performance electrochemical CO_2 reduction: unravelling the roles of N-doping†

Jian Zhu,‡[a] Jing Hu,‡[c] Zhenyu Wang,[c] Zhouguang Lu,[c] Shoubhik Das *[ab] and Pegie Cool *[a]

Doping strategies have been recognized as effective approaches for developing cost-effective and durable catalysts with enhanced reactivity and selectivity in the electrochemical synthesis of value-added compounds directly from CO_2. However, the reaction mechanism and the specific roles of heteroatom doping, such as N doping, in advancing the CO_2 reduction reaction are still controversial due to the lack of precise control of catalyst surface microenvironments. In this study, we investigated the effects of N doping on the performances for electrochemically converting CO_2 to CO over Ni@NCNT/graphene hybrid structured catalysts (Ni@NCNT/Gr). Ni nanoparticles (Ni NPs) were encapsulated in N-doped carbon nanotubes (NCNTs) which were *in situ* generated from g-C_3N_4 during the annealing process due to the thermal catalysis of the existing Ni NPs. Our results show that the optimized pyrrolic N doping level, coupled with stable NCNT/Gr hybrid structures, high electrochemically active surface area, rich active sites, and reduced Ni NP size, synergistically contribute to the distinguished electrocatalytic performances. The as-prepared Ni@NCNT/Gr-R catalyst demonstrated a high CO faradaic efficiency (>90%) with negligible differences in CO FE across a wide potential range (−0.71–−0.91 V *vs.* RHE) in an H-cell while maintaining magnificent stability with negligible current density loss for 24 hours at −0.71 V (*vs.* RHE). Our findings provide evidence and insight into the optimization of pyrrolic N doping levels together with reducing NP size within the stable NCNT/Gr hybrid substrate for designing efficient CO_2 reduction catalysts.

Received 30th October 2024
Accepted 6th January 2025

DOI: 10.1039/d4sc07354a

rsc.li/chemical-science

1 Introduction

Recently, converting CO_2 into value-added products powered by renewable energies has become highly attractive due to their sustainable nature. Among the developed technologies, the electrochemical CO_2 reduction reaction (ECO2RR) represents the most promising strategy to realize a carbon-neutral or carbon-net cycle by converting CO_2 into commodity chemicals and transportation fuels.[1–3] However, applying the ECO2RR to the industry is hampered by low selectivity and reactivity due to its complicated reaction mechanism, sluggish reaction kinetics, and competitive hydrogen evolution reaction.[4–7] To avoid these, recently, transition metal-based catalysts including Fe, Co, and Ni have emerged as the most promising candidates with the advantages of their natural abundance and electronic structure tunability by chelating with heteroatoms at an atomic scale.[8–13] Especially, N-doping plays significant roles in tuning the geometric and electronic properties of the metal center, particularly at the interfaces between the active center and doped N atoms.[14–17] Indeed, a few heteroatom-doped catalysts have demonstrated high CO selectivity and reactivity far surpassing those of the hydrogen evolution reaction (HER). For example, Li *et al.* demonstrated a high CO faradaic efficiency (FE) of >90% in a wide potential range on an exclusive four pyridinic-N coordinated Ni single atom catalyst.[18] Liu *et al.* have designed a model pyrrolic-N coordinated Ni single atom catalyst which exhibited a maximum CO FE of 99% at a low overpotential of 600 mV.[19] In addition, single atom catalysts with various lower or higher coordination numbers also presented high CO selectivity of >90%.[20–22] However, the ECO2RR performance varies dramatically with the changes in the microenvironment; for instance, a decreased coordination number offers more unoccupied 3d orbitals, which enhances CO_2 adsorption,

[a]*Department of Chemistry, University of Antwerp, Antwerp 2610, Belgium. E-mail: Pegie.Cool@uantwerpen.be*

[b]*Department of Chemistry, University of Bayreuth, Bayreuth 95447, Germany. E-mail: Shoubhik.Das@uni-bayreuth.de*

[c]*Department of Materials Science and Engineering, Southern University of Science and Technology, Shenzhen 518055, PR China*

† Electronic supplementary information (ESI) available. See DOI: https://doi.org/10.1039/d4sc07354a

‡ These authors contributed equally.

and thus lowers the energy that is required for the formation of the *COOH intermediate, and improves the selectivity in product formation.[23] However, the clear roles of different types of N configurations are still under debate; especially, the reaction mechanism over nanoparticle (NPs) catalysts decorated on a specific N-doped carbon substrate has rarely been investigated.[24–27]

It should be also noted that electrode architecture has great influence on the electrochemical performances as well, which governs the accessibility of active sites and mass/electron transport.[28–30] Over the past few decades, carbon nanotubes (CNTs) and graphene (Gr) as ideal substrates have been extensively studied by virtue of their high electronic conductivity and structural stability.[31,32] Cheng and co-workers reported that a Ni-based single atom catalyst, dispersed on CNTs, displayed a CO selectivity of 91.3% and high partial current of 23.5 mA cm^{-2}.[33] Furthermore, Wang *et al.* synthesized an intrinsic defect-rich graphene-like carbon dispersed with Fe-single sites by pyrolyzing g-C_3N_4, which displayed a high CO faradaic efficiency of 90% and high j_{CO} of 33 mA cm^{-2}.[34] However, direct loading of Ni-atoms onto CNTs is quite challenging due to the steady structure of CNTs which results in a low atom loading (Fig. 1a).[35] Moreover, low electrochemically active surface area (ECSA) of graphene at the gas/liquid/solid three-phase interface is usually observed because two-dimensional (2D) graphene layers are prone to stack together due to the strong π–π interaction between ultrathin graphene layers (Fig. 1b).[36,37] Therefore, catalysts with excellent architectures that can provide rich active sites and lead to high selectivity and reactivity are highly desired.

Considering all of this, we have rationally designed an N-doped carbon nanotube/graphene (NCNT/Gr) hybrid structured catalyst decorated with Ni NPs by carbonizing g-C_3N_4 with the assistance of polyvinylpyrrolidone (PVP). The Ni NPs catalyze the *in situ* formation of N-doped CNTs (NCNTs) during the calcination process and meanwhile, the Ni NPs were encapsulated in the formed NCNTs. In the hybrid structured Ni@NCNT/Gr catalysts, consequently, Gr with a high specific surface area serves as a scaffold which is beneficial for the CO_2 adsorption; NCNTs act as an electron conductive skeleton while preventing Gr layers' stacking to some extent and provide active sites for the ECO2RR at the Ni/NCNT interface. Benefiting from the distinguished hybrid structure, the Ni@NCNT/Gr-800 hybrid catalyst with an optimal pyrrolic N-doping level displayed a much-improved CO selectivity and reactivity in a gas-tight H-cell (Fig. 1c). Furthermore, density functional theory (DFT) clarifies that the pyrrolic N lowered the reaction energy at the rate determining step which facilitated the reaction kinetics of the ECO2RR. After further reduction of the particle size, Ni@NCNT/Gr-R exhibits high CO FEs > 90% in a wide overpotential range of 300 mV with the highest CO FE of 94.5% at −0.71 V (all the potentials in this study were converted to the reversible hydrogen electrode (RHE) scale unless otherwise stated) and an outstanding catalytic durability at −0.71 V for 24 h.

2 Results and discussion

2.1 Microstructure of the hybrid structured Ni@NCNT/Gr catalysts

The Ni@NCNT/Gr catalysts were prepared by loading the Ni^{2+} salt onto the g-C_3N_4 followed by covering with PVP (polyvinylpyrrolidone). Then, the final products were obtained by carbonizing the PVP@Ni@g-C_3N_4 precursors at various

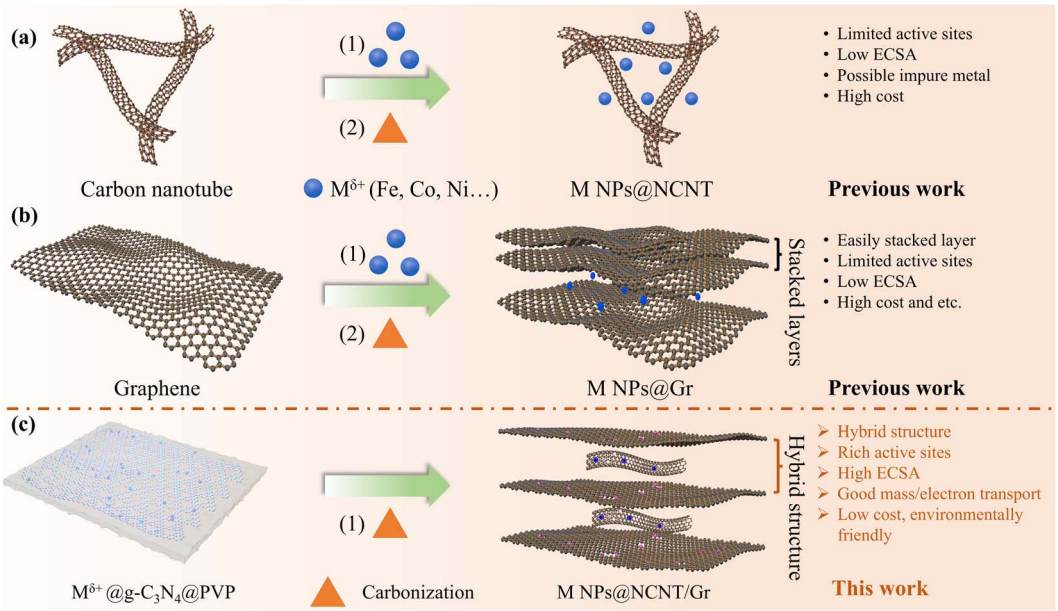

Fig. 1 (a and b) Representation of carbon nanotubes (CNTs) and graphene (Gr) decorated with nanoparticles for electrochemical CO_2 reduction; (c) overview of the synthesis strategy of Ni@NCNT/Gr catalysts in this work.

temperatures ($T = 700$, 800, 900 °C) followed by acid etching for 24 h (Fig. 2a). During the calcination process, the Ni NPs catalyzed the *in situ* formation of NCNTs and meanwhile, the Ni NPs were encapsulated in the formed NCNTs.[38] In addition, PVP is transformed into graphene-like layers. To explore the obtained compositions after the synthesis of the catalysts, XRD patterns of the hybrid Ni@NCNT/Gr catalysts obtained at different temperatures were collected (Fig. 2b). The three sharp diffraction peaks located at 44.5°, 51.8°, and 76.4° are assigned to the (111), (200), and (220) facets of metallic Ni (JCPDS# 04-0850). The peak centered at 26.0° is indexed to the (002) plane of carbon and the intensity is increased with temperature, indicating an increased graphitization degree of the NCNT/Gr substrate which was formed by the catalysis of Ni during calcination.[39,40] The intensity of Ni@NCNT/Gr-700 is much lower than that of its counterparts indicating a low crystallization degree. In addition, the shoulder peak at 47.4° in the Ni@NCNT/Gr-700 sample is attributed to the (103) plane of g-C_3N_4 due to the insufficient carbonization.[41] Furthermore, Raman spectroscopy was employed to describe the defect degree of the NCNT/Gr hybrid structure. As displayed in Fig. 2c, four bands are observed at 1220, 1346, 1473 and 1584 cm^{-1}, corresponding to the D4, D1, D3 and G bands of carbon substrates, respectively. The D1 and D4 bands are assigned to the A_{1g} symmetry vibrational modes of a disordered graphitic lattice, where D1 is related to the amorphous carbon, while D4 arises from polyene structures or ionic impurities. The D3 band is associated with stacking faults and turbostratic structures, while the G band arises from the E_{2g} symmetry vibration of a perfect graphitic lattice.[42–44] The D/G intensity ratio (I_{D1}/I_G) reflects the degree of defect density of the carbon substrate.[45,46] Among those three samples collected at various temperatures, Ni@NCNT/Gr-800 shows a high I_{D1}/I_G value of 1.07, indicating a high defect concentration that resulted from the high N-doping level.[47] The I_{D1}/I_G is decreased to 1.0 with further increasing the calcination temperature to 900 °C, which is attributed to a higher graphitization degree with a lower N doping concentration due to the decomposition of the relatively

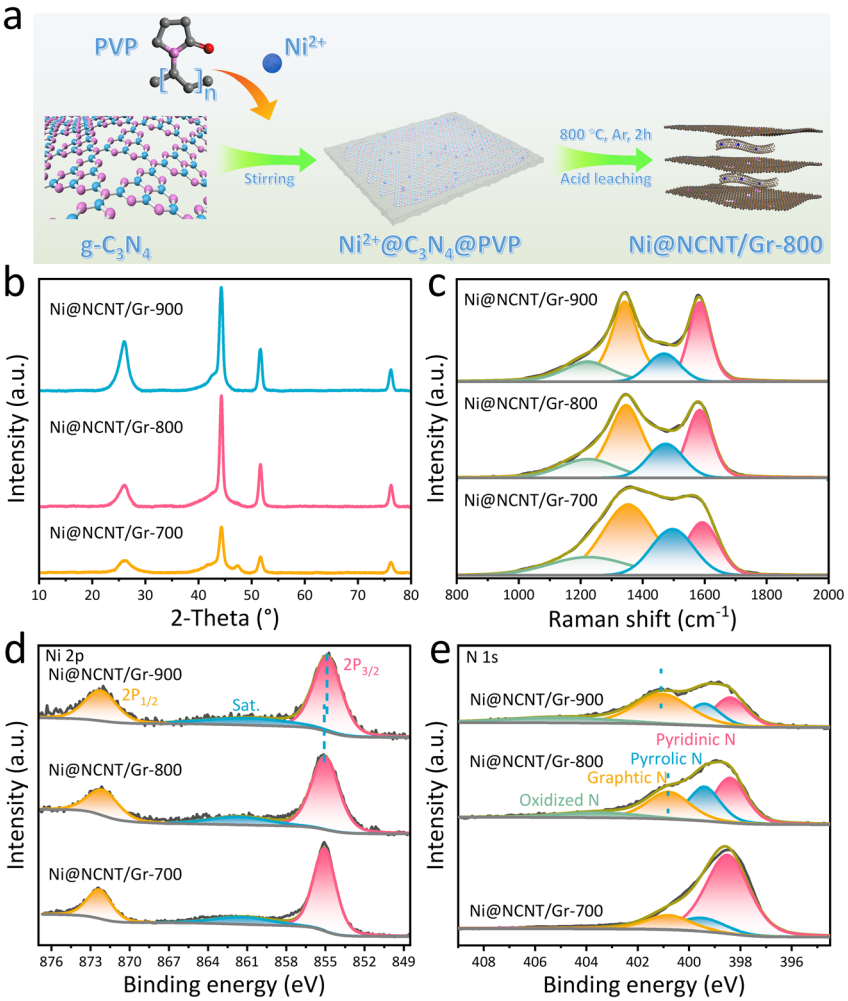

Fig. 2 (a) Schematic illustration of the preparation route of the Ni@NCNT/Gr-800 catalysts; (b) XRD patterns; (c) Raman spectra; (d) high-resolution Ni 2p XPS spectra; (e) high resolution N 1s XPS spectra of the Ni@NCNT/Gr-T ($T = 700$, 800, and 900 °C) catalysts.

unstable N-containing motifs, which is in line with the XRD results.[48,49] However, the highest I_{D1}/I_G value (1.3) is obtained at 700 °C, which is assigned to the much higher N doping level due to the insufficient graphitization of the g-C_3N_4.[50] By comparing the mathematical area of the deconvoluted D and G bands, as displayed in Fig. S1,† the D band percentage (D4 + D1 + D3) decreases with the applied temperature due to the decrease of amorphous carbon content, which implies an increased graphitization degree. Thus, the broad Raman peak in Ni@NCNT/Gr-700 is assigned to the relatively higher amount of amorphous carbon. Additionally, N_2 adsorption–desorption isotherms were recorded to determine the specific surface area and porosity. The as-obtained Ni@NCNT/Gr-*T* catalysts that were obtained at various temperatures suggest comparable specific surface areas with only a few variations and show similar diameters, whereas the meso-macropores decreased with the increase of annealing temperature (Fig. S2†).

To explore the chemical state of the as-obtained catalysts, X-ray photoelectron spectroscopy (XPS) was applied, and no other elements are observed other than C, N, O, and Ni in the survey spectrum (Fig. S3†). The binding energy of the Ni $2p_{3/2}$ in Fig. 2d increases from 854.9 eV to 855.1 eV but is lower than 855.8 eV when the temperature is increased to 900 °C, indicating that the valence state of Ni is between 0 and +2.[51–53] The peaks located between Ni $2p_{1/2}$ and Ni $2p_{3/2}$ are assigned to the satellite peaks of Ni $2p_{3/2}$.[54] The high-resolution N 1s XPS spectra of Ni@NCNT/Gr-700 can be deconvoluted into three peaks at 398.4 eV, 399.4 eV, and 400.8 eV, corresponding to pyridinic N, pyrrolic N, and graphitic N, respectively (Fig. 2e).[55–57] While Ni takes part in the carbonization, it can stabilize carbon by interacting with nitrogen atoms, thus avoiding the rapid loss of the small nitrogen source during the calcination process, guaranteeing carbon formation, and transforming pyridinic N into pyrrolic N and graphitic N.[39] When the calcination temperature is increased to 800 °C, the pyridinic N percentage notably reduces from 73.2 at% to 35.3 at%, while the percentage of pyrrolic N centered at 399.4 eV is significantly increased from 13.1 at% to 26.6 at% (Fig. S4†). It is well known that N configuration has a substantial impact on the electrochemical reactivity of the resulting materials. Regarding the electron configuration of N in the carbon substrate, pyrrolic N with a lone pair of electrons perpendicular to the graphene plane increases electron density to a large extent and thus results in abundant absorptive sites.[58,59] However, the total N content decreases to 9.2 at% that is much lower than that of Ni@NCNT/Gr-700 (28.9 at%), further confirming the decomposition of the unstable structures of N-containing motifs at a high temperature.[60] A new peak is observed at 403.5 eV, which can be attributed to oxidized N.[61] By increasing the temperature to 900 °C, the graphitic N peak is shifted to higher binding energies (from 400.8 eV to 401.1 eV) and the percentage increases strikingly up to 42.9 at%, indicating an increased graphitization degree.[62,63] The increased graphitic N can accelerate electron transfer and improve the conductivity of the carbon substrate due to its unique micro-environment.[64] However, the pyridinic N and pyrrolic N drop significantly when the total N at% decreases to 6.2 at%, consistent with the increased graphitization degree confirmed by the XRD result in Fig. 2b.

The morphology of the as-obtained Ni@NCNT/Gr-800 catalyst was investigated by transmission electron microscopy (TEM). As can be seen in Fig. 3a–c, an NCNT/Gr hybrid structure is observed with particle size mainly distributed in the range of 20–40 nm (accounting for ~80% of the particles). No lattice fringes are observed either in the low magnification or high-resolution TEM images (HRTEM) due to the coverage of NCNTs on Ni nanoparticles. The 2D graphene-like layers

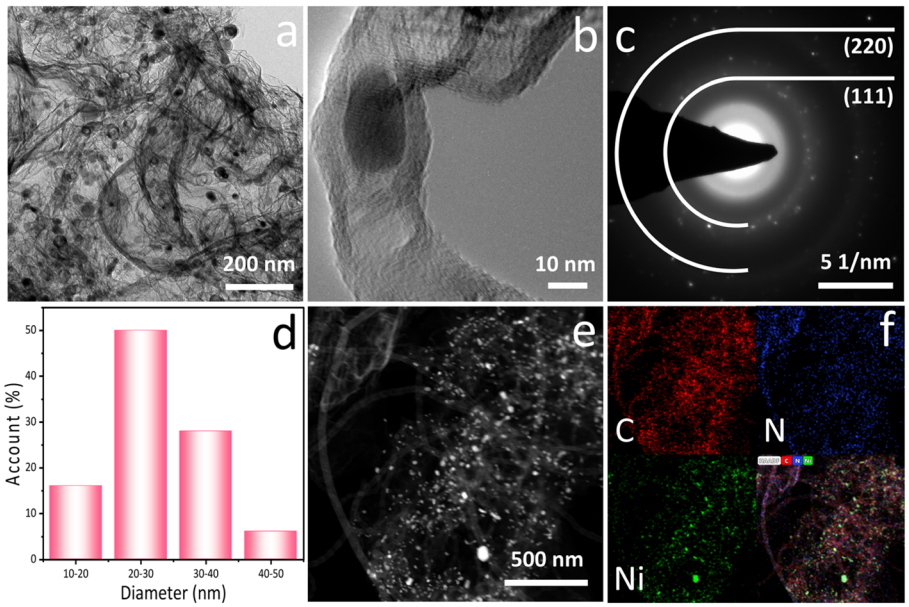

Fig. 3 (a and b) TEM and HRTEM images; (c) SAED pattern; (d) particle size distribution; (e and f) HAADF-STEM images of the as-prepared Ni@NCNT/Gr-800 catalyst.

originate from the carbonization of the coated PVP. The NCNTs are *in situ* formed resulting from the carbonization of g-C_3N_4 by the thermal catalysis of the Ni NPs, and Ni NPs are encapsulated in the NCNTs at the same time.[65] The selected area electron diffraction (SAED) pattern in Fig. 3c indicates that the diffraction patterns can be indexed to the (220) and (111) facets of Ni, suggesting high purity of the obtained product. The energy-dispersive X-ray spectroscopy (EDX) images in Fig. 3e and f demonstrate that bright dots can be related to Ni, while the N and C are homogeneously distributed throughout the selected area. These results indicate that the hybrid structured Ni@NCNT/Gr catalysts are fabricated successfully.

2.2 Electrocatalytic activity of Ni@NCNT/Gr catalysts

After detailed characterization of the as-synthesized catalysts, we investigated the ECO2RR selectivity and reactivity for the hybrid catalytic Ni@NCNT/Gr materials. The products were detected and analyzed by on-line gas chromatography (GC) and 1H nuclear magnetic resonance (^{1}H NMR). CO and H_2 are the only products, and no liquid product was detected (Fig. S5†). Firstly, linear sweep voltammetry (LSV) was conducted in a N_2 and CO_2 saturated 0.5 M $KHCO_3$ solution in a gas-tight H-cell. As shown in Fig. 4a, the Ni@NCNT/Gr-800 and Ni@NCNT/Gr-900 display much higher total current density (j_{total}) in the CO_2-saturated electrolyte than that in N_2-saturated electrolyte, which clearly suggests higher activities towards the ECO2RR. Moreover, N-doped carbon (NC) shows a much inferior current density response and more negative onset potential than the Ni@NCNT/Gr-800 catalyst indicating that Ni nanoparticles are the active sites and effect of single-atom catalyst is ruled out (Fig. S6 and S7†). As a result, the Ni@NCNT/Gr-800 suggests a high CO faradaic efficiency (FE_{CO}) of 87.8% with a partial current density (j_{CO}) of 27.9 mA cm^{-2} at −0.81 V, which is higher than that of a Ni@NCNT/Gr-900 catalyst as demonstrated in Fig. 4b and c. The superior ECO2RR performances of Ni@NCNT/Gr-800 can be attributed to the differences in the content of doped N. More specifically, the enhancement of CO selectivity and reactivity is attributed to the higher pyrrolic N doping level which possesses a lone pair electron and results in a higher electron density. In contrast, the Ni@NCNT/Gr-700 displayed much inferior ECO2RR reactivity but a high HER reactivity in Fig. S8† despite its high N content according to the XPS results. The low ECO2RR reactivity of Ni@NCNT/Gr-700 is attributed to the insufficient carbonization of the g-C_3N_4/PVP precursor. In addition, the reaction kinetics of the ECO2RR on the as-prepared samples were further evaluated by the Tafel slope, which connects the increase in overpotential with the logarithm of the j_{CO}. Similar Tafel slopes of 147.7 and 151 mV dec^{-1} are observed in Ni@NCNT/Gr-800 and Ni@NCNT/Gr-900 in Fig. 4d, which are smaller than 188.8 mV dec^{-1} for Ni@NCNT/Gr-700 and comparable with the catalysts listed in Table S1,† implying fast kinetics. In addition, a higher ECSA is suggested in Ni@NCNT/Gr-800 (Fig. 4e and S9†), which arises from higher pyrrolic N content that can lead to richer absorptive sites. Moreover, the smaller resistance of Ni@NCNT/Gr-800 and Ni@NCNT/Gr-900 in electrochemical impedance spectrum (EIS) in Fig. 4f is attributed to the increased graphitic N, which can accelerate electron transfer and improve the conductivity of the carbon substrate due to its unique microenvironment.

Besides, the effects of PVP on the ECO2RR performances were also investigated, Ni@NCNT/Gr-*x*PVP (x = 1, 2, 3) with different amounts of PVP were prepared at 800 °C, as demonstrated in the

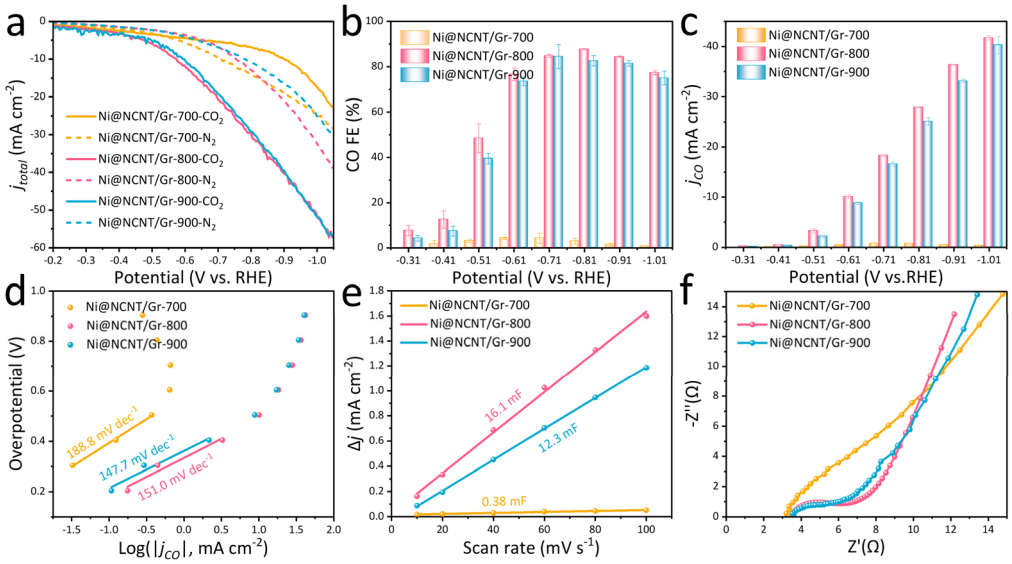

Fig. 4 ECO2RR performances of the Ni@NCNT/Gr-*T* catalysts. (a) LSV curves in N_2 and CO_2 saturated 0.5 M $KHCO_3$ at a scan rate of 10 mV s^{-1}; (b and c) the CO FEs and CO partial current densities at independent potentials from −0.31–−1.01 V (*vs.* RHE); (d) Tafel plots of polarization overpotential (η) *versus* CO partial current density of Ni@NCNT/Gr-*T* (T = 700, 800, 900 °C) catalysts; (e) charging current density differences plotted against scan rates, roughness factor (RF) was calculated from the ratio of ECSA on the electrode to the geometric area of the carbon paper electrode. Roughness factor values of Ni@NCNT/Gr-700, Ni@NCNT/Gr-800, and Ni@NCNT/Gr-900 electrodes are 805, 615, and 19, respectively; (f) Nyquist plots of the as-prepared catalysts at the open circuit potential (OCP).

experimental section. As shown in Fig. S10a and b,† the as-prepared samples show no impurities other than Ni and carbon substrate, and Raman spectra imply that Ni NPs are supported on the N-doped carbon substrate. Although a high difference in specific surface area is observed in Fig. S10c,† the porosity diameter remained (Fig. S10d†). When evaluating the samples under the same conditions as Ni@NCNT/Gr-*T* catalysts, the Ni@NCNT/Gr-2PVP catalyst that was prepared by following the same procedure as that for the Ni@NCNT/Gr-800 displays the highest ECO2RR reactivity and selectivity as shown in Fig. S11a–c.† The relatively higher ECO2RR may originate from the higher ECSA, which can provide more active sites and thus lead to high CO selectivity and reactivity (Fig. S11d and S12†).

To further upgrade the ECO2RR performances, a refined catalyst defined as Ni@NCNT/Gr-R was prepared under the same conditions as the Ni@NCNT/Gr-800 catalyst but with loading less Ni^{2+} for the PVP@Ni@g-C_3N_4 precursor. As a result, the as-prepared Ni@NCNT/Gr-R shows a clearer NCNT/Gr hybrid structure encapsulated with Ni NPs in the NCNTs. However, the particle size is reduced with the three highest contributions being in the range between 10 and 25 nm (Fig. S13†). The diffraction rings in the SAED pattern can be indexed to the (111) and (220) facets of metallic Ni, respectively, which are consistent with the XRD and TEM results of Ni@NCNT/Gr-800. XRD was applied to explore the purities of the refined Ni@NCNT/Gr-R catalyst; three distinct diffraction peaks located at 44.5°, 51.8°, and 76.4° are observed, which are assigned to the (111), (200), and (220) facets of metallic Ni (JCPDS# 04-0850), respectively (Fig. S14a†). The intense peak at 26° is attributed to the (002) facet of graphitic carbon and no other impurities are detected.[39] The Raman spectrum was recorded to reveal the graphitization degree (Fig. S14b†); a high I_{D1}/I_G value of 1.09 is obtained, which is in line with the Ni@NCNT/Gr-800 catalyst with a high defect concentration.[47] High-resolution XPS spectra of N and Ni were employed to explore the chemical state (Fig. S11c and d†). However, the total N content increased to 15.4% when compared with Ni@NCNT/Gr-800, which is assigned to a lower graphitization degree resulting from the reduced Ni content that can catalyze the formation of graphitic carbon during the annealing process.[53,55] To reveal the chemical state, as depicted in Fig. S14c,† the four peaks at 398.4, 399.2, 400.8, and 403.5 eV can be assigned to pyridinic N, pyrrolic N, graphitic N, and oxidized N, respectively.[55] Fig. S14d† reveals three peaks of Ni $2p_{1/2}$, Ni $2p_{3/2}$, and Ni sat. of the Ni@NCNT/Gr-R catalyst at 872.3, 855.1, and 861.8 eV, respectively, which is in good agreement with the result of Ni@NCNT/Gr-800 indicating that the valence state of Ni remained stable after reducing the nanoparticles' diameter.[52,53] The content of Ni in the Ni@NCNT/Gr-R is determined to be 6.6% by ICP-MS.

To explore the ECO2RR performances, electrochemical tests were conducted under the same conditions as those of the Ni@NCNT/Gr-*T* and Ni@NCNT/Gr-*x*PVP samples. As shown in Fig. 5a, Ni@NCNT/Gr-R displays a higher ECO2RR activity in a CO_2-saturated electrolyte than in an N_2-saturated electrolyte as presented by the LSV curves. In addition, Ni@NCNT/Gr-R demonstrates the highest CO FE of 94.5% at −0.71 V which is higher and slightly more positive than that of the Ni@NCNT/Gr-800 catalyst. Moreover, Ni@NCNT/Gr-R shows little difference in CO FEs in the potential range of −0.71–−0.91 V with a high

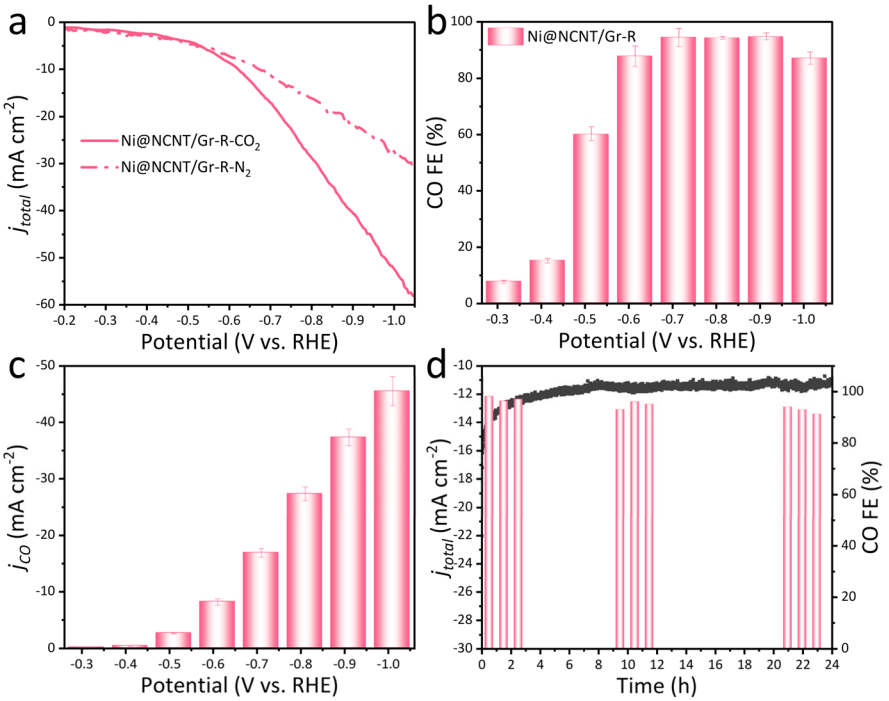

Fig. 5 ECO2RR performances of the Ni@NCNT/Gr-R catalysts. (a) LSV curves in N_2 and CO_2 saturated 0.5 M $KHCO_3$ at a scan rate of 10 mV s^{-1}; (b and c) the CO FEs and CO partial current densities at independent potentials from −0.31 to −1.01 V (*vs.* RHE); (d) electrocatalytic stability test at −0.71 V in CO_2-saturated 0.5 M $KHCO_3$.

j_{CO} of −37.4 mA cm^{-2} at −0.91 V in Fig. 5b and c, which is much higher than those of Ni@NCNT/Gr-*T* and Ni@NCNT/Gr-*x*PVP catalysts, and is comparable with the recently reported advanced catalysts as listed in Table S1.† The enhancement in CO selectivity and reactivity is attributed to the reduced Ni nanoparticle size which can provide a richer adsorption site with a high surface/volume ratio, like corner and edge sites, for the key intermediate of *COOH and *CO, and thus promote the formation of CO.[61,66,67] Moreover, Ni@NCNT/Gr-R exhibits outstanding electrocatalytic stability for 24 h and CO FEs remain higher than 90% with little current density loss at −0.71 V in Fig. 5d. The enhanced CO selectivity is attributed to synergistic effects of the reduced NP size and optimal pyrrolic N doping concentration when compared with Ni@NCNT/Gr-800. More specifically, optimal pyrrolic N doping increases charge density and exposed active sites for absorbing intermediates, and the reduced particle diameter provides more active sites with the reactant, which synergistically contributes to the high performances of the ECO2RR. In addition, the NCNT/Gr hybrid structure remained stable after long-term electrocatalysis as evidenced by TEM analysis displayed in Fig. S15,† certifying an exceptional durability of the hybrid electrode structure under the conditions of electrolysis for a period of 24 h.

2.3 Theoretical calculation and mechanism of Ni@NCNT/Gr catalysts

To investigate the mechanism on Ni@NCNT/Gr-R, the Tafel slope in Fig. 6a illustrates a slightly faster kinetics for Ni@NCNT/Gr-R when comparing with Ni@NCNT/Gr-800 (see Fig. 4d), which is indexed to the higher adsorption sites. Furthermore, Ni@NCNT/Gr-R displays a higher electrochemical active surface area in Fig. 6b, which results from the relatively higher pyrrolic N doping level at a high active site concentration after reducing the Ni NP size, which is helpful for intermediate adsorption and further reduction.

To further understand the underlying mechanism of the N-doping effects on the ECO2RR on Ni@NCNT/Gr catalysts, DFT calculations were performed using the Materials Studio program. Fig. S16 and S17† display the optimized models with adsorption of *COOH and *CO on various Ni@NC sites. The ECO2RR pathways on Ni@NCNT/Gr catalysts are proposed and generally consist of a consecutive two proton-coupled electron transfer process starting with CO_2 adsorption, and the formation of the *COOH intermediate by the first proton-coupled electron process and the subsequent formation of the *CO intermediate. The last step is the desorption of the *CO intermediate.[68] According to the experimental results, the Gibbs free energy (ΔG) changes of the key *COOH and *CO intermediates on various N moieties were evaluated. As shown in Fig. S19a,† DFT calculation certifies that the ECO2RR is facilitated on a pyrrolic N doped graphene catalyst with the adsorption of CO_2 onto the active site as the rate determining step, which is more favorable (1.97 eV) when compared with pure graphene (2.99 eV). Metallic Ni shows a much more thermally and kinetically favorable process at the beginning of the ECO2RR, whereas a much higher activation energy (2.68 eV) is required for *CO desorption at the rate

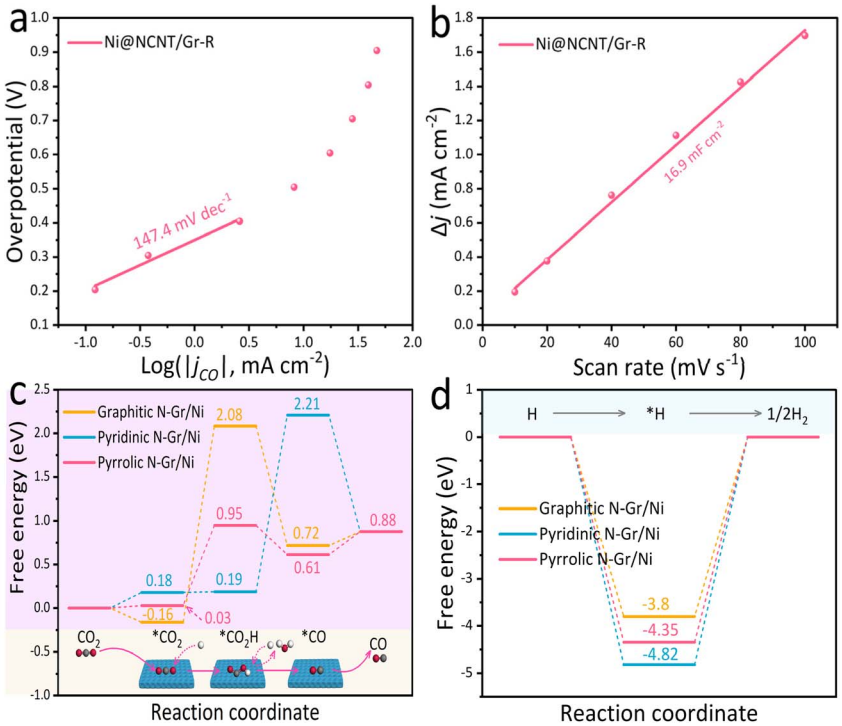

Fig. 6 (a) Tafel plots of polarization overpotential (η) *versus* CO partial current density of Ni@NCNT/Gr-R; (b) charging current density differences plotted against scan rates, the roughness factor is 845; (c) free energy diagrams for ECO2RR pathways on graphitic N-Gr-Ni, pyridinic N-Gr/Ni, and pyrrolic N-Gr/Ni; (d) the calculated free energy diagrams for the HER to H_2 on graphitic N-Gr-Ni, pyridinic N-Gr/Ni, and pyrrolic N-Gr/Ni.

determining step due to the strong binding strength with *CO, which retards the ECO2RR. Therefore, combining N doped carbon and a transition metal is promising. As shown in Fig. 6c, the transformation of $*CO_2$ into *COOH can be easily realized on pyridinic N-Gr/Ni due to its negligible difference in ΔG (0.01 eV). However, for the step of *CO desorption, the rate-determining step, a large free energy barrier of 2.02 eV is observed for pyridinic N-Gr/Ni. In contrast, the desorption of the *CO intermediate occurs spontaneously on graphitic N-Gr/Ni and pyrrolic N-Gr/Ni catalysts. The formation of the *COOH intermediate is the rate-determining step for graphitic N-Gr/Ni and pyrrolic N-Gr/Ni, whereas the free energy path of the formation of *COOH on the pyrrolic N-Gr/Ni site is thermodynamically more favorable (0.92 eV) in comparison with that on graphitic N-Gr/Ni (2.24 eV). The enhanced adsorption to *COOH may originate from the lone pair electron on the pyrrolic N site which induces charge redistribution and increases the electron density on the adjacent atoms. The enhanced electron density at the pyrrolic N-C sites promotes CO_2 adsorption, thereby accelerating the ECO2RR process.[69,70] This result is consistent with our experimental results that Ni@NCNT/Gr-800 with the highest pyrrolic N-doping level shows the best CO FE% and reactivity. Meanwhile, the HER as the main side reaction was also considered in the calculation (Fig. S18†). As displayed in Fig. 6d and S19b,† pure graphene and pyrrolic N-Gr are thermodynamically favorable for the HER under CO_2 reduction conditions. Metallic Ni is the most unfavorable catalyst for the HER under the CO_2 reduction conditions. When integrating N-doped carbon and the transition metal simultaneously, although *H can be formed more easily, a much higher energy barrier has to be overcome for graphitic N-Gr/Ni (3.8 eV), pyridinic N-Gr/Ni (4.82 eV) and pyrrolic N-Gr/Ni (4.35 eV) when compared with pure carbon (0.26 eV), N-doped carbon (2.51 eV) and metallic Ni (3.95 eV). Therefore, the pyrrolic N-Gr/Ni is verified to be the kinetically most unfavorable for the HER due to the high energy barrier. Moreover, the difference between the limiting potentials for CO_2 reduction and H_2 evolution ($U_L(CO_2) - U_L(H_2)$) can serve as a descriptor, where a more positive $U_L(CO_2) - U_L(H_2)$ value indicates a better product selectivity towards the ECO2RR.[71,72] As shown in Fig. S20,† the $U_L(CO_2) - U_L(H_2)$ values for graphitic N-Gr/Ni, pyrrolic N-Gr/Ni and pyridinic N-Gr/Ni are 1.56, 3.43 and 2.8, respectively, which implies that pyrrolic N-Gr/Ni possesses the highest CO selectivity, consistent with the electrochemical results. Considering all the above parameters, pyrrolic N-Gr/Ni with an optimal pyrrolic N doping level is proven to be the most promising catalyst for the ECO2RR due to its much more positive limiting potential and relatively lower energy barrier (0.92 eV) than those of pyridinic N-Gr/Ni (2.02 eV) and graphitic N-Gr/Ni (2.24 eV) at the rate-determining step for the formation of the *COOH intermediate and higher energy barrier for the HER.

3 Conclusions

In summary, a series of hybrid NCNT/Gr catalysts were prepared with *in situ* encapsulated Ni nanoparticles for electrochemical CO_2 reduction. By changing the carbonization temperature, Ni@NCNT/Gr-800 with the optimized pyrrolic N doping level displayed the highest CO selectivity and reactivity. The electrochemical CO_2 reduction performances were further improved due to the decreased Ni NP size and increased N doping concentration in the Ni@NCNT-Gr-R catalyst, which displayed high CO faradaic efficiencies higher than 90% in an overpotential range of 300 mV and suggested distinguished electrocatalytic stability for 24 h. Furthermore, by combining DFT calculations, the unexpectedly high ECO2RR performances were attributed to the synergetic effects of the optimal pyrrolic N doping and the reduced particle size, which increased charge density, lowered energy barrier, and exposed abundant active sites. In addition, the stable hybrid NCNT/Gr substrate can facilitate mass/electron transport, maximize the active site distribution, and prevent the Ni nanoparticles from reacting with the electrolyte. The interesting synthesis strategy that we applied produces very active Ni@NCNT/Gr hybrid catalysts which clearly provide new opportunities for effective ECO2RR conversion by precise design of the catalyst and N-heteroatom doping, which plays an important role.

Data availability

The data supporting this article have been included as part of the ESI.†

Author contributions

J. Z. conceptualized the project. P. C. and S. D. supervised the project. J. Z. synthesized the catalysts, conducted the catalytic experiments and the related data processing, and performed materials characterization and analysis. J. H. and Z. W conducted TEM measurement and DFT calculations and analysed the corresponding results. Z. L. edited and review the manuscript.

Conflicts of interest

The authors declare that they have no known competing financial interests or personal relationships that could have appeared to influence the work reported in this paper.

Acknowledgements

This work was financially supported by the Chinese Scholarship Council (CSC No. 202008440279). P. Cool acknowledges funding from the Moonshot Vlaio project (SYNCAT) and the BOF-TOP project from the University of Antwerp. The authors would like to acknowledge Mr Thomas Kenis from the ELCAT group for the ICP-MS measurements.

Notes and references

1 M. Mikkelsen, M. Jørgensen and F. C. Krebs, The teraton challenge. A review of fixation and transformation of carbon dioxide, *Energy Environ. Sci.*, 2010, **3**(1), 43–81.
2 Y. Y. Birdja, E. Pérez-Gallent, M. C. Figueiredo, A. J. Göttle, F. Calle-Vallejo and M. T. M. Koper, Advances and

challenges in understanding the electrocatalytic conversion of carbon dioxide to fuels, *Nat. Energy*, 2019, **4**(9), 732–745.

3 T.-J. Wang, W.-S. Fang, Y.-M. Liu, F.-M. Li, P. Chen and Y. Chen, Heterostructured Pd/PdO nanowires for selective and efficient CO_2 electroreduction to CO, *J. Energy Chem.*, 2022, **70**, 407–413.

4 D. Gao, R. M. Arán-Ais, H. S. Jeon and C. B. Roldan, Rational catalyst and electrolyte design for CO_2 electroreduction towards multicarbon products, *Nat. Catal.*, 2019, **2**(3), 198–210.

5 M. B. Ross, P. De Luna, Y. Li, C.-T. Dinh, D. Kim, P. Yang and E. H. Sargent, Designing materials for electrochemical carbon dioxide recycling, *Nat. Catal.*, 2019, **2**(8), 648–658.

6 J. Han, X. Bai, X. Xu, X. Bai, A. Husile, S. Zhang, L. Qi and J. Guan, Advances and challenges in the electrochemical reduction of carbon dioxide, *Chem. Sci.*, 2024, **15**(21), 7870–7907.

7 F. Hao, Y. Wang and Z. Fan, Rational design of single-atom catalysts for electrochemical carbon dioxide reduction toward multi-carbon products, *Energy Lab.*, 2023, **1**(2), 220023.

8 H. Mistry, A. S. Varela, S. Kühl, P. Strasser and B. R. Cuenya, Nanostructured electrocatalysts with tunable activity and selectivity, *Nat. Rev. Mater.*, 2016, **1**(4), 16009.

9 Q. Wang, Y. Lei, D. Wang and Y. Li, Defect engineering in earth-abundant electrocatalysts for CO_2 and N_2 reduction, *Energy Environ. Sci.*, 2019, **12**(6), 1730–1750.

10 X. Li, L. Liu, X. Ren, J. Gao, Y. Huang and B. Liu, Microenvironment modulation of single-atom catalysts and their roles in electrochemical energy conversion, *Sci. Adv.*, 2020, **6**(39), 6833–6856.

11 K. Li, S. Zhang, X. Zhang, S. Liu, H. Jiang, T. Jiang, C. Shen, Y. Yu and W. Chen, Atomic Tuning of Single-Atom Fe-N-C Catalysts with Phosphorus for Robust Electrochemical CO_2 Reduction, *Nano Lett.*, 2022, **22**(4), 1557–1565.

12 M. Qu, Z. Chen, Z. Sun, D. Zhou, W. Xu, H. Tang, H. Gu, T. Liang, P. Hu, G. Li, *et al.*, Rational design of asymmetric atomic Ni-P_1N_3 active sites for promoting electrochemical CO_2 reduction, *Nano Res.*, 2022, **16**(2), 2170–2176.

13 J. Zhu, T. Mulder, A. Rokicińska, L. M. Lindenbeck, R. W. A. Havenith, A. Cunha, P. Kuśtrowski, A. Slabon, S. Das and P. Cool, Synergistic Interaction Between Ni-Center and Glycine-derived N-doped Porous Carbon Material Boosts Electrochemical CO_2 Reduction, *ACS Catal.*, 2024, **14**(14), 10987–10997.

14 Z. Chen, A. Huang, K. Yu, T. Cui, Z. Zhuang, S. Liu, J. Li, R. Tu, K. Sun, X. Tan, *et al.*, Fe_1N_4-O_1 site with axial Fe-O coordination for highly selective CO_2 reduction over a wide potential range, *Energy Environ. Sci.*, 2021, **14**(6), 3430–3437.

15 C. Jia, X. Tan, Y. Zhao, W. Ren, Y. Li, Z. Su, S. C. Smith and C. Zhao, Sulfur-Dopant-Promoted Electroreduction of CO_2 over Coordinatively Unsaturated Ni-N_2 Moieties, *Angew. Chem., Int. Ed.*, 2021, **60**(43), 23342–23348.

16 H. K. Lim, H. Shin, W. A. Goddard III, Y. J. Hwang, B. K. Min and H. Kim, Embedding covalency into metal catalysts for efficient electrochemical conversion of CO_2, *J. Am. Chem. Soc.*, 2014, **136**(32), 11355–11361.

17 S. Liang, J. Xiao, T. Zhang, Y. Zheng, Q. Wang and B. Liu, Sulfur Changes the Electrochemical CO_2 Reduction Pathway over Cu Electrocatalysts, *Angew. Chem., Int. Ed.*, 2023, **62**(44), e202310740.

18 X. Li, W. Bi, M. Chen, Y. Sun, H. Ju, W. Yan, J. Zhu, X. Wu, W. Chu, C. Wu, *et al.*, Exclusive Ni-N_4 Sites Realize Near-Unity CO Selectivity for Electrochemical CO_2 Reduction, *J. Am. Chem. Soc.*, 2017, **139**(42), 14889–14892.

19 S. Liu, H. B. Yang, S. F. Hung, J. Ding, W. Cai, L. Liu, J. Gao, X. Li, X. Ren, Z. Kuang, *et al.*, Elucidating the Electrocatalytic CO_2 Reduction Reaction over a Model Single-Atom Nickel Catalyst, *Angew. Chem., Int. Ed.*, 2020, **59**(2), 798–803.

20 Y. Pan, R. Lin, Y. Chen, S. Liu, W. Zhu, X. Cao, W. Chen, K. Wu, W. C. Cheong, Y. Wang, *et al.*, Design of Single-Atom Co-N_5 Catalytic Site: A Robust Electrocatalyst for CO_2 Reduction with Nearly 100% CO Selectivity and Remarkable Stability, *J. Am. Chem. Soc.*, 2018, **140**(12), 4218–4221.

21 X. Wang, Z. Chen, X. Zhao, T. Yao, W. Chen, R. You, C. Zhao, G. Wu, J. Wang, W. Huang, *et al.*, Regulation of Coordination Number over Single Co Sites: Triggering the Efficient Electroreduction of CO_2, *Angew. Chem., Int. Ed.*, 2018, **57**(7), 1944–1948.

22 C. Yan, H. Li, Y. Ye, H. Wu, F. Cai, R. Si, J. Xiao, S. Miao, S. Xie, F. Yang, *et al.*, Coordinatively unsaturated nickel–nitrogen sites towards selective and high-rate CO_2 electroreduction, *Energy Environ. Sci.*, 2018, **11**(5), 1204–1210.

23 N. Wang, H. Li, H. Wang, H. Yang, Z. Ren and R. Xu, Temperature-Induced Low-Coordinate Ni Single-Atom Catalyst for Boosted CO_2 Electroreduction Activity, *Small*, 2023, **19**(35), e2301469.

24 M. Jia, C. Choi, T. S. Wu, C. Ma, P. Kang, H. Tao, Q. Fan, S. Hong, S. Liu, Y. L. Soo, *et al.*, Carbon-supported Ni nanoparticles for efficient CO_2 electroreduction, *Chem. Sci.*, 2018, **9**(47), 8775–8780.

25 F. Wang, Z. Miao, J. Mu, Y. Zhao, M. Liang, J. Meng, X. Wu, P. Zhou, J. Zhao, S. Zhuo, *et al.*, A Ni nanoparticles encapsulated in N-doped carbon catalyst for efficient electroreduction CO_2: Identification of active sites for adsorption and activation of CO_2 molecules, *Chem. Eng. J.*, 2022, **428**, 131323.

26 M. Liang, Y. Liu, J. Zhang, F. Wang, Z. Miao, L. Diao, J. Mu, J. Zhou and S. Zhuo, Understanding the role of metal and N species in M@NC catalysts for electrochemical CO_2 reduction reaction, *Appl. Catal., B*, 2022, **306**, 121115.

27 Y. Gang, E. Sarnello, J. Pellessier, S. Fang, M. Suarez, F. Pan, Z. Du, P. Zhang, L. Fang, Y. Liu, *et al.*, One-Step Chemical Vapor Deposition Synthesis of Hierarchical Ni and N Co-Doped Carbon Nanosheet/Nanotube Hybrids for Efficient Electrochemical CO_2 Reduction at Commercially Viable Current Densities, *ACS Catal.*, 2021, **11**(16), 10333–10344.

28 A. B. Jorge, R. Jervis, A. P. Periasamy, M. Qiao, J. Feng, L. N. Tran and M. M. Titirici, 3D Carbon Materials for Efficient Oxygen and Hydrogen Electrocatalysis, *Adv. Energy Mater.*, 2019, **10**(11), 1902494.

29 D. C. Higgins, M. A. Hoque, F. Hassan, J.-Y. Choi, B. Kim and Z. Chen, Oxygen Reduction on Graphene–Carbon Nanotube Composites Doped Sequentially with Nitrogen and Sulfur, *ACS Catal.*, 2014, **4**(8), 2734–2740.

30 B.-Q. Miao, W.-S. Fang, B. Sun, F.-M. Li, X.-C. Wang, B.-Y. Xia and Y. Chen, Defect-rich bismuth metallene for efficient CO_2 electroconversion, *Chin. J. Struct. Chem.*, 2023, **42**(8), 100095.

31 H. Wang, T. Maiyalagan and X. Wang, Review on Recent Progress in Nitrogen-Doped Graphene: Synthesis, Characterization, and Its Potential Applications, *ACS Catal.*, 2012, **2**(5), 781–794.

32 C. Hu and L. Dai, Doping of Carbon Materials for Metal-Free Electrocatalysis, *Adv. Mater.*, 2019, **31**(7), e1804672.

33 Y. Cheng, S. Zhao, B. Johannessen, J. P. Veder, M. Saunders, M. R. Rowles, M. Cheng, C. Liu, M. F. Chisholm, M. R. De, *et al.*, Atomically Dispersed Transition Metals on Carbon Nanotubes with Ultrahigh Loading for Selective Electrochemical Carbon Dioxide Reduction, *Adv. Mater.*, 2018, **30**(13), e1706287.

34 W. Ni, Z. Liu, Y. Zhang, C. Ma, H. Deng, S. Zhang and S. Wang, Electroreduction of Carbon Dioxide Driven by the Intrinsic Defects in the Carbon Plane of a Single Fe-N_4 Site, *Adv. Mater.*, 2021, **33**(1), e2003238.

35 S. Zhang, P. Yue, Y. Zhou, J. Li, X. Zhu, Q. Fu and Q. Liao, Ni Single Atoms Embedded in Graphene Nanoribbon Sieves for High-Performance CO_2 Reduction to CO, *Small*, 2023, **19**(43), e2303016.

36 F. Pan, B. Li, E. Sarnello, Y. Fei, Y. Gang, X. Xiang, Z. Du, P. Zhang, G. Wang, H. T. Nguyen, *et al.*, Atomically Dispersed Iron-Nitrogen Sites on Hierarchically Mesoporous Carbon Nanotube and Graphene Nanoribbon Networks for CO_2 Reduction, *ACS Nano*, 2020, **14**(5), 5506–5516.

37 V. Georgakilas, J. N. Tiwari, K. C. Kemp, J. A. Perman, A. B. Bourlinos, K. S. Kim and R. Zboril, Noncovalent Functionalization of Graphene and Graphene Oxide for Energy Materials, Biosensing, Catalytic, and Biomedical Applications, *Chem. Rev.*, 2016, **116**(9), 5464–5519.

38 Y. Zhang, R. Jiang, Z. Wang, Y. Xue, J. Sun and Y. Guo, (Fe,N-codoped carbon nanotube)/(Fe-based nanoparticle) nanohybrid derived from Fe-doped g-C_3N_4: A superior catalyst for oxygen reduction reaction, *J. Colloid Interface Sci.*, 2020, **579**, 391–400.

39 Y. Ding, C. Yu, J. Chang, C. Yao, J. Yu, W. Guo and J. Qiu, Effective Fixation of Carbon in g-C_3N_4 Enabled by Mg-Induced Selective Reconstruction, *Small*, 2020, **16**(10), e1907164.

40 M. Liang, Y. Liu, H. Huang, L. Diao, J. Mu, Z. Miao, J. Zhou and S. Zhuo, A robust Ni@NCNT-C catalyst for highly efficient electrochemical CO_2 reduction to CO over a wide potential range, *Chem. Eng. J.*, 2022, **450**, 137962.

41 J. Xu, Y. Qi and L. Wang, In situ derived Ni_2P/Ni encapsulated in carbon/g-C_3N_4 hybrids from metal–organic frameworks/g-C_3N_4 for efficient photocatalytic hydrogen evolution, *Appl. Catal., B*, 2019, **246**, 72–81.

42 J.-J. Cai, Q.-Y. Zhou, X.-F. Gong, B. Liu, Y.-L. Zhang, Y.-K. Dai, D.-M. Gu, L. Zhao, X.-L. Sui and Z.-B. Wang, Metal-free amino acid glycine-derived nitrogen-doped carbon aerogel with superhigh surface area for highly efficient Zn-Air batteries, *Carbon*, 2020, **167**, 75–84.

43 A. Sadezky, H. Muckenhuber, H. Grothe, R. Niessner and U. Pöschl, Raman microspectroscopy of soot and related carbonaceous materials: Spectral analysis and structural information, *Carbon*, 2005, **43**(8), 1731–1742.

44 C. Marino, J. Cabanero, M. Povia and C. Villevieille, Biowaste Lignin-Based Carbonaceous Materials as Anodes for Na-Ion Batteries, *J. Electrochem. Soc.*, 2018, **165**(7), A1400–A1408.

45 J. Yan, H. Meng, F. Xie, X. Yuan, W. Yu, W. Lin, W. Ouyang and D. Yuan, Metal free nitrogen doped hollow mesoporous graphene-analogous spheres as effective electrocatalyst for oxygen reduction reaction, *J. Power Sources*, 2014, **245**, 772–778.

46 W. Yuan, Y. Zhou, Y. Li, C. Li, H. Peng, J. Zhang, Z. Liu, L. Dai and G. Shi, The edge- and basal-plane-specific electrochemistry of a single-layer graphene sheet, *Sci. Rep.*, 2013, **3**, 2248.

47 M. R. Ammar, N. Galy, J. N. Rouzaud, N. Toulhoat, C. E. Vaudey, P. Simon and N. Moncoffre, Characterizing various types of defects in nuclear graphite using Raman scattering: Heat treatment, ion irradiation and polishing, *Carbon*, 2015, **95**, 364–373.

48 S. Yang, X. Feng, X. Wang and K. Mullen, Graphene-based carbon nitride nanosheets as efficient metal-free electrocatalysts for oxygen reduction reactions, *Angew. Chem., Int. Ed.*, 2011, **50**(23), 5339–5343.

49 J. Luo, K. Wang, X. Hua, W. Wang, J. Li, S. Zhang and S. Chen, Pyridinic-N Protected Synthesis of 3D Nitrogen-Doped Porous Carbon with Increased Mesoporous Defects for Oxygen Reduction, *Small*, 2019, **15**(11), e1805325.

50 F. Besharat, F. Ahmadpoor, Z. Nezafat, M. Nasrollahzadeh, N. R. Manwar, P. Fornasiero and M. B. Gawande, Advances in Carbon Nitride-Based Materials and Their Electrocatalytic Applications, *ACS Catal.*, 2022, **12**(9), 5605–5660.

51 H. B. Yang, S.-F. Hung, S. Liu, K. Yuan, S. Miao, L. Zhang, X. Huang, H.-Y. Wang, W. Cai, R. Chen, *et al.*, Atomically dispersed Ni(i) as the active site for electrochemical CO_2 reduction, *Nat. Energy*, 2018, **3**(2), 140–147.

52 C.-Z. Yuan, H.-B. Li, Y.-F. Jiang, K. Liang, S.-J. Zhao, X.-X. Fang, L.-B. Ma, T. Zhao, C. Lin and A.-W. Xu, Tuning the activity of N-doped carbon for CO_2 reduction *via in situ* encapsulation of nickel nanoparticles into nano-hybrid carbon substrates, *J. Mater. Chem. A*, 2019, **7**(12), 6894–6900.

53 C. F. Wen, F. Mao, Y. Liu, X. Y. Zhang, H. Q. Fu, L. R. Zheng, P. F. Liu and H. G. Yang, Nitrogen-Stabilized Low-Valent Ni Motifs for Efficient CO_2 Electrocatalysis, *ACS Catal.*, 2019, **10**(2), 1086–1093.

54 Q. Lu, C. Chen, Q. Di, W. Liu, X. Sun, Y. Tuo, Y. Zhou, Y. Pan, X. Feng, L. Li, *et al.*, Dual Role of Pyridinic-N Doping in Carbon-Coated Ni Nanoparticles for Highly Efficient Electrochemical CO_2 Reduction to CO over a Wide Potential Range, *ACS Catal.*, 2022, **12**(2), 1364–1374.

55 S. Liang, Q. Jiang, Q. Wang and Y. Liu, Revealing the Real Role of Nickel Decorated Nitrogen-Doped Carbon Catalysts

for Electrochemical Reduction of CO_2 to CO, *Adv. Energy Mater.*, 2021, **11**(36), 2101477.

56 Y. Wang, B. J. Park, V. K. Paidi, R. Huang, Y. Lee, K.-J. Noh, K.-S. Lee and J. W. Han, Precisely Constructing Orbital Coupling-Modulated Dual-Atom Fe Pair Sites for Synergistic CO_2 Electroreduction, *ACS Energy Lett.*, 2022, **7**(2), 640–649.

57 D. M. Koshy, S. Chen, D. U. Lee, M. B. Stevens, A. M. Abdellah, S. M. Dull, G. Chen, D. Nordlund, A. Gallo, C. Hahn, *et al.*, Understanding the Origin of Highly Selective CO_2 Electroreduction to CO on Ni,N-doped Carbon Catalysts, *Angew. Chem., Int. Ed.*, 2020, **59**(10), 4043–4050.

58 Y. Tang, X. Wang, J. Chen, X. Wang, D. Wang and Z. Mao, PVP-assisted synthesis of g–C_3N_4–derived N-doped graphene with tunable interplanar spacing as high-performance lithium/sodium ions battery anodes, *Carbon*, 2021, **174**, 98–109.

59 J. Liu, Y. Zhang, L. Zhang, F. Xie, A. Vasileff and S. Z. Qiao, Graphitic Carbon Nitride (g-C_3N_4)-Derived N-Rich Graphene with Tuneable Interlayer Distance as a High-Rate Anode for Sodium-Ion Batteries, *Adv. Mater.*, 2019, **31**(24), 1901261.

60 K. Chizari, A. Vena, L. Laurentius and U. Sundararaj, The effect of temperature on the morphology and chemical surface properties of nitrogen-doped carbon nanotubes, *Carbon*, 2014, **68**, 369–379.

61 Z. Li, D. He, X. Yan, S. Dai, S. Younan, Z. Ke, X. Pan, X. Xiao, H. Wu and J. Gu, Size-Dependent Nickel-Based Electrocatalysts for Selective CO_2 Reduction, *Angew. Chem., Int. Ed.*, 2020, **59**(42), 18572–18577.

62 Y. Xia and R. Mokaya, Generalized and Facile Synthesis Approach to N-Doped Highly Graphitic Mesoporous Carbon Materials, *Chem. Mater.*, 2005, **17**(6), 1553–1560.

63 S. Zhang, S. Tsuzuki, K. Ueno, K. Dokko and M. Watanabe, Upper limit of nitrogen content in carbon materials, *Angew. Chem., Int. Ed.*, 2015, **54**(4), 1302–1306.

64 Z. Zhang, Y. Zhang, X. Mu, J. Du, H. Wang, B. Huang, J. Zhou, X. Pan and E. Xie, The carbonization temperature effect on the electrochemical performance of nitrogen-doped carbon monoliths, *Electrochim. Acta*, 2017, **242**, 100–106.

65 X. Liu, W. Yang, L. Chen, Z. Liu, L. Long, S. Wang, C. Liu, S. Dong and J. Jia, Graphitic Carbon Nitride (g-C_3N_4)-Derived Bamboo-Like Carbon Nanotubes/Co Nanoparticles Hybrids for Highly Efficient Electrocatalytic Oxygen Reduction, *ACS Appl. Mater. Interfaces*, 2020, **12**(4), 4463–4472.

66 D. Gao, H. Zhou, J. Wang, S. Miao, F. Yang, G. Wang, J. Wang and X. Bao, Size-dependent electrocatalytic reduction of CO_2 over Pd nanoparticles, *J. Am. Chem. Soc.*, 2015, **137**(13), 4288–4291.

67 C. Kim, H. S. Jeon, T. Eom, M. S. Jee, H. Kim, C. M. Friend, B. K. Min and Y. J. Hwang, Achieving Selective and Efficient Electrocatalytic Activity for CO_2 Reduction Using Immobilized Silver Nanoparticles, *J. Am. Chem. Soc.*, 2015, **137**(43), 13844–13850.

68 P. Prslja and N. López, Stability and Redispersion of Ni Nanoparticles Supported on N-Doped Carbons for the CO_2 Electrochemical Reduction, *ACS Catal.*, 2020, **11**(1), 88–94.

69 R. Boppella, P. M. Austeria, Y. Kim, E. Kim, I. Song, Y. Eom, D. P. Kumar, M. Balamurugan, E. Sim, D. H. Kim, *et al.*, Pyrrolic N-Stabilized Monovalent Ni Single-Atom Electrocatalyst for Efficient CO_2 Reduction: Identifying the Role of Pyrrolic-N and Synergistic Electrocatalysis, *Adv. Funct. Mater.*, 2022, **32**(35), 2202351.

70 H. B. Yang, J. Miao, S.-F. Hung, J. Chen, H. B. Tao, X. Wang, L. Zhang, R. Chen, J. Gao, H. M. Chen, *et al.*, Identification of catalytic sites for oxygen reduction and oxygen evolution in N-doped graphene materials: Development of highly efficient metal-free bifunctional electrocatalyst, *Sci. Adv.*, 2016, **2**(4), e1501122.

71 D. Kim, C. Xie, N. Becknell, Y. Yu, M. Karamad, K. Chan, E. J. Crumlin, J. K. Norskov and P. Yang, Electrochemical Activation of CO_2 through Atomic Ordering Transformations of AuCu Nanoparticles, *J. Am. Chem. Soc.*, 2017, **139**(24), 8329–8336.

72 W. Bi, X. Li, R. You, M. Chen, R. Yuan, W. Huang, X. Wu, W. Chu, C. Wu and Y. Xie, Surface Immobilization of Transition Metal Ions on Nitrogen-Doped Graphene Realizing High-Efficient and Selective CO_2 Reduction, *Adv. Mater.*, 2018, **30**(18), e1706617.